



# Unprecedented enhancement in strength-plasticity synergy of (TiC+Al<sub>6</sub>MoTi+Mo)/Al cermet by multiple length-scale microstructure stimulated synergistic deformation

Hong-Yu Yang<sup>a,b,c</sup>, Yi-Fan Yan<sup>a,b</sup>, Tian-Shu Liu<sup>a,b</sup>, Bai-Xin Dong<sup>a,b</sup>, Liang-Yu Chen<sup>c</sup>, Shi-Li Shu<sup>a,d</sup>, Feng Qiu<sup>a,b,\*</sup>, Qi-Chuan Jiang<sup>a,b</sup>, Lai-Chang Zhang<sup>e,\*\*</sup>

<sup>a</sup> State Key Laboratory of Automotive Simulation and Control, Jilin University, PR China

<sup>b</sup> Key Laboratory of Automobile Materials, Ministry of Education and Department of Materials Science and Engineering, Jilin University, Renmin Street NO. 5988, Changchun, Jilin Province, 130025, PR China

<sup>c</sup> National Demonstration Center for Experimental Materials Science and Engineering Education, Jiangsu University of Science and Technology, Zhenjiang, 212003, PR China

<sup>d</sup> School of Mechanical and Aerospace Engineering, Jilin University, Renmin Street NO. 5988, Changchun, Jilin Province, 130025, PR China

<sup>e</sup> School of Engineering, Edith Cowan University, 270 Joondalup Drive, Joondalup, Perth, WA, 6027, Australia

## ARTICLE INFO

### Keywords:

Metal-ceramic composites  
Strength-plasticity synergy  
Multiple length-scale microstructure  
Stress concentration delocalization  
Deformation compatibility

## ABSTRACT

Metal-ceramic composites generally exhibit limited strength-plasticity synergy due to pronounced difference in elastic and plastic deformation between “soft phase” and “hard phase”, bottlenecking their applications. This work proposes a novel microstructure design concept using refractory metals and intermetallics to offer compromises between “soft phase” and “hard phase”. A cost-effective fabrication method was used to produce 70 vol % (TiC + Al<sub>6</sub>MoTi + Mo)/Al cermet. The cermet is composed of submicron-TiC, micron-Al<sub>6</sub>MoTi and nano-Mo particles separated by Al in homogeneous microstructure. This multiple length-scale microstructure could delocalize stress concentration, enhance work hardening and deformation compatibility in cermet, resulting in unprecedentedly enhanced strength-plasticity synergy. Ultimate compressive strength, plastic strain and product of strength and plasticity of (TiC + Al<sub>6</sub>MoTi + Mo)/Al at room temperature and 573 K respectively are 1227 MPa, 6.9%, 7445 MPa-% and 781 MPa, 15.0%, 10021 MPa-%, which are increased by ~30%, ~25%, ~60% and ~37%, ~9%, 41% respectively compared with those for traditional 70 vol% TiC/Al. This work opens new perspectives for the design and application of metal-ceramic composites with high strength and plasticity synergy.

## 1. Introduction

Achieving strength-plasticity synergy is a focus and difficult scientific problem in structural materials [1–4]. With increasing requirements from light weight and safety considerations [5,6], a wide range of design concepts of microstructure have been proposed [7–11]. Lei et al. [12] reported enhanced strength-ductility of 316L stainless steel by pre-formed gradient nanostructured surface layer. Li et al. [13] and Xiong et al. [14] revealed that nano-twin microstructure incorporated by plastic deformation could enhance resistance to interface cracking and strength-fracture toughness in steels. Furthermore, inspired by

nature, metal-ceramic composites (MMCs), which are composed of “soft phase” and “hard phase” with “brick-and-mortar” microstructure, have infused new vigor into strength-plasticity synergy [15–19]. However, the significant difference in elastic and plastic deformation between “soft phase” and “hard phase” would trigger interface debonding [20, 21], which is the main failure mode of such composites. Hence, such composites, even with a well-crafted biomimetic hierarchical or gradient microstructure, usually exhibit mechanical properties far below their theoretical ones. Furthermore, the content of hard phases in biomimetic composites is much lower than that in natural materials (~95 vol%). On the other hand, the preparation of such composites

\* Corresponding author. Key Laboratory of Automobile Materials, Ministry of Education and Department of Materials Science and Engineering, Jilin University, Renmin Street NO. 5988, Changchun, Jilin Province, 130025, PR China.

\*\* Corresponding author.

E-mail addresses: [qiufeng@jlu.edu.cn](mailto:qiufeng@jlu.edu.cn) (F. Qiu), [lczhangimr@gmail.com](mailto:lczhangimr@gmail.com), [lzhang@ecu.edu.au](mailto:lzhang@ecu.edu.au) (L.-C. Zhang).

<https://doi.org/10.1016/j.compositesb.2021.109265>

Received 21 July 2021; Received in revised form 25 August 2021; Accepted 27 August 2021

Available online 28 August 2021

1359-8368/© 2021 Elsevier Ltd. All rights reserved.

requires complex processing, e.g. freezing casting, freeze drying and high-temperature sintering of ceramic scaffolds, and pressure infiltration of molten metal [18]. For instance, Sun et al. [22] fabricated Al/Al<sub>2</sub>O<sub>3</sub> composites with a nacre-inspired “brick-and-mortar” structure. Although the composite exhibits an excellent bending strength, the bending strength increases while fracture toughness decreases from 138 MPa m<sup>1/2</sup> to 41 MPa m<sup>1/2</sup> as the Al<sub>2</sub>O<sub>3</sub> content increases from 8 vol% to 48 vol%. Hu et al. [23] constructed Cu/(TiC–Cr<sub>3</sub>C<sub>2</sub>) composites with a laminate-reticular architecture, the composites exhibit declining damage-tolerant properties with enhancing the ceramic content from 30 vol% to 34 vol%. The cracking of ceramic layers and debonding of ceramic/metal interfaces emerged in the composite with 34 vol% ceramic at low stress level. Thus, the strength-plasticity trade-off has not yet been solved in MMCs. In addition, Radi et al. [24] suggested to search for strategies for improving the design of MMCs.

The current research team has been making considerable endeavors to solving the interface debonding problem by enhancing interface bonding strength between ceramics and metals [25,26]. Although the increase in interface bonding strength can enhance the mechanical property of composites and somewhat refrain interfacial debonding, the strong interface bonding can only alter the propagation direction of cracks, i.e. from along the interface to Al matrix, yet cannot improve the deformation incompatibility between ceramics and metals. As such, the crack source induced by stress concentration is still present at the interface. Furthermore, it is well known that nacre has three structures, i.e. cuticle, prismatic and nacreous layers [27]. Because each structure is composed of aragonite and biopolymer, nacre displays a microstructure with hard, soft and hardest phases [28]. In this regard, this work proposes a novel microstructure design concept, using refractory metals and intermetallics, which offers some compromises between brittle TiC and ductile Al, as a bridge to collaboratively deform the MMCs, to constitute multiple length-scale microstructure in new composites. Among the refractory metals, refractory metal Mo is known to play a positive role in determining the properties of MMCs [29]. According to Al–Mo phase diagram [30], Mo is prone to form intermetallic with Al. Therefore, a single-step fabrication method by cost-effective in situ reaction hot-pressing was used in this work to produce the 70 vol% TiC/Al cermet with and without Mo addition, respectively. Furthermore, the microstructure and mechanical property at room temperature and 573 K (which is the upper limit for use) of the cermets were contrastively analyzed, the mechanisms of strengthening and toughening for the cermet are critically discussed. This work shows that this novel strategy can achieve unprecedented strength-plasticity synergy.

## 2. Experimental

The fabrication process is shown in Fig. 1a and Fig. 1b. The commercial pure Al powder (99.7 wt% purity, ~25 μm), Mo powder (99.9 wt% purity, ~15 μm), Ti powder (99.5 wt% purity, ~25 μm) and CNTs powder (≥95.0 wt% purity, diameter: 8–15 nm, length: 30–50 μm) were used as the raw materials. These powders were mixed by ball milling at a

speed of 40 rpm for 24 h (Fig. 1a). Afterward, the mixed powder was put into a graphite mold in a vacuum furnace and a pre-pressure of 2 MPa was applied, then mixed powder was heated at a heating rate of about 30 K/min (Fig. 1b). When the powder was heated to about 879 K, the reaction of cermet synthesis accompanied by a massive heat release started and hard-phase particles were formed as a product instantaneously under the coverage of liquid Al. Meanwhile, an optimized pressure was applied to the reacting powder for 20 s. Finally, the heating process was stopped, and the product was furnace-cooled to room temperatures. In the synthesis process of cermet, the temperature of the reaction system rapidly rose to about 2640 K owing to the heat release of reaction, which reached the liquidus in Al–Mo phase diagram [30]. This facilitated Mo to further diffuse uniformly and participate in the reaction. Meanwhile, the reinforcements obtained in the processing were refined and homogeneously dispersed, and the heterogeneous phase interfaces were clean and with high thermal stability, which is attributed to the preparation method of in situ reaction hot-pressing [31]. Finally, the cermets were successfully prepared. For convenience, the 70 vol% TiC/Al cermets with and without Mo additions were named as TA-M and TA respectively hereafter.

The phase constituents of the cermets were examined by X-ray diffraction (XRD) using a Rigaku D/Max 2500 PC diffractometer with Cu K<sub>α</sub> radiation. The dislocation density ( $\rho$ ) is evaluated using the XRD diffraction profiles. The Williamson-Hall method [32,33] was used in the calculation of  $\rho$ , and the details was described in Refs. [34,35]. The microstructures, elemental mappings and fracture surface morphologies of the cermets were examined by an Evo18 Carl Zeiss scanning electron microscope (SEM) with energy dispersive spectrometry (EDS). The crystallographic mismatch and possible orientation relationships (ORs) between phases in the cermets were predicted by the edge-to-edge model (E2EM) [36,37]. The calculation method of interplanar spacing mismatch ( $f_d$ ) between close or nearly close packed planes in phases and interatomic spacing mismatch ( $f_i$ ) along possible directions among phases was described in Refs. [25,38,39]. The morphology of ceramic particles, which were extracted from the cermets using 18 vol% HCl ethanol solutions, was observed by a JSM6700F field emission SEM. The crystallographic characteristics of phase were determined by a JEM-2100F transmission electron microscope (TEM), and the interfaces between particles and Al in the cermets were examined by high resolution TEM. The mechanical properties were evaluated by quasistatic uniaxial compression tests at room temperature and 573 K (which is the upper limit for use) respectively in an MTS 810 servo-hydraulic testing machine. The elastic modulus ( $E$ ) was measured using the ultrasonic pulse echo technique.

## 3. Results and discussion

### 3.1. Microstructure

Fig. 1c shows the XRD diffraction patterns for the TA and TA-M. The TA is composed of TiC and  $\alpha$ -Al in microstructure. By contrast, in

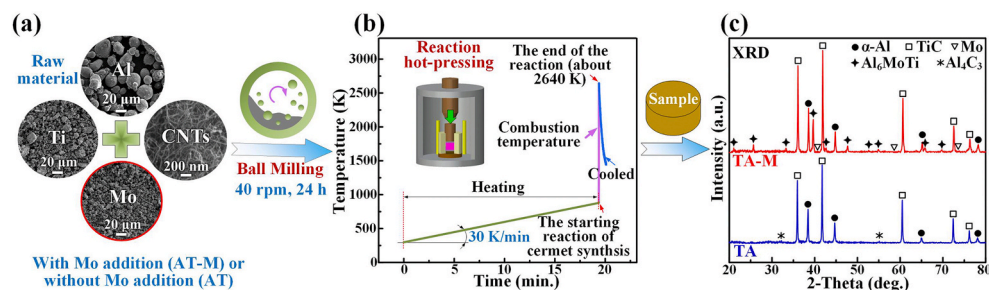


Fig. 1. (a) and (b) fabrication process of cermets and technical parameters, (c) XRD patterns for the prepared cermets. TA-M and TA are 70 vol% TiC/Al cermets with and without Mo addition, respectively.

addition to TiC and  $\alpha$ -Al,  $Al_6MoTi$  and trace Mo are detected in TA-M. Furthermore, the SEM micrographs of the cermetes shown in Fig. 2 indicate that the submicron spherical particles with an average diameter of 0.5  $\mu m$  are uniformly distributed in both cermetes. The spherical particles are detected as Ti and C by EDS (Fig. 2a). However, a small number of columnar particles about 1  $\mu m$  in length are randomly distributed in the TA-M, and the columnar particles are composed of Al, Ti and Mo (Fig. 2b). According to EDS mappings of the selected area in TA-M, unreacted Mo is uniform distributed in the TA-M (Fig. 2c).

The orientation relationships with minimum mismatch between phases in the TA and TA-M are shown in Fig. 3. The values of interplanar spacing mismatch ( $f_d$ ) and interatomic spacing mismatch ( $f_r$ ) between  $\alpha$ -Al and TiC in TA are 6.35%. However, the values of  $f_d$  and  $f_r$  between  $\alpha$ -Al and  $Al_6MoTi$  in TA-M respectively are 2.88% and 0.50%, between Mo and  $Al_6MoTi$  in TA-M respectively are 2.22% and 1.09%, and between Mo and TiC in TA-M respectively are 2.88%. Consequently, the  $f_d$  and  $f_r$  between phases in TA-M are lower than the corresponding ones in TA. By the way, the minimum values of  $f_d$  and  $f_r$  between  $\alpha$ -Al and TiC are slightly different in TA and TA-M. This is because the lattice parameters of  $\alpha$ -Al and TiC in TA are different from the corresponding ones in TA-M which contains Mo in raw material. Low crystallographic mismatch facilitates the formation of low-energy and stability interface, which is favor to interfacial bonding. Meanwhile, low crystallographic mismatch may cause large distortion energy and increase dislocation density in cermet. The dislocation density calculated by the Williamson–Hall method [32,33] is  $3.5 \times 10^{14} m^{-2}$  and  $5.7 \times 10^{14} m^{-2}$  in TA and TA-M, respectively. High dislocation density is beneficial to dislocation interaction and accumulation at reinforcement particles. The dislocation accumulation produces work hardening and the strain hardening rate largely determines the uniform deformation [40–42]. Therefore, both high interfacial bonding and dislocation density are beneficial to the compatible deformation of cermetes [43].

Fig. 4a–c shows the TEM micrographs of the cermetes. For the TA, the dark spherical particles are separated by light-color areas (Fig. 4a), and they are respectively identified as face-centered cubic (FCC) TiC and  $\alpha$ -Al by selected area electron diffraction (SAED) patterns. For the TA-M, the dark-color spherical particles and columnar particle in the TA-M

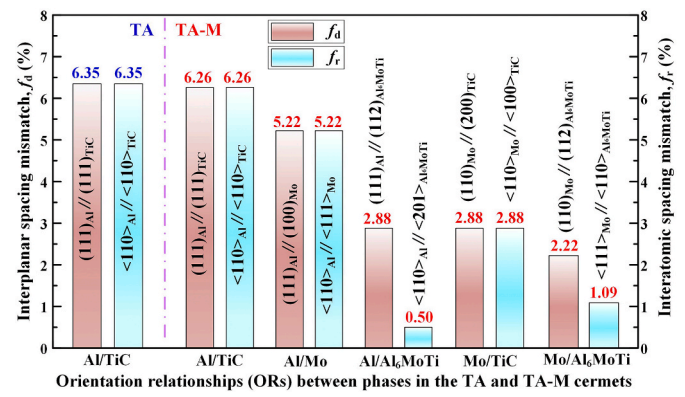


Fig. 3. The orientation relationships with minimum mismatch between phases in the TA and TA-M.

(Fig. 4b and c) are identified as TiC and tetragonal ( $I4/mmm$ )  $Al_6MoTi$  respectively. In addition, the nano-particles (region “c<sub>2</sub>” in Fig. 4c) are also identified as body-centered cubic (BCC) Mo. The interfaces between  $\alpha$ -Al and TiC or  $Al_6MoTi$  are clean and well-bonded (Fig. 4a<sub>3</sub>, b<sub>3</sub> and c<sub>3</sub>). Hence, the schematic diagrams of microstructural configuration of the TA and TA-M are shown in Fig. 4d and e. The microstructural configuration of the TA displays that submicron TiC particles are evenly dispersed and separated by Al. By contrast, the microstructural configuration of the TA-M displays that the particles are in multiple length scales and are composed of randomly distributed submicron-TiC, micron intermetallic  $Al_6MoTi$  and nano-Mo particles. Therefore, the TA-M has a homogenous multiple length-scales microstructure.

### 3.2. Mechanical properties

Fig. 5a<sub>1</sub> and Fig. 5b<sub>1</sub> respectively show the uniaxial compressive engineering stress-strain curves for both cermetes. The compressive properties of TA-M are significantly greater than the corresponding ones of TA. The mechanical properties are summarized in Table 1. As seen

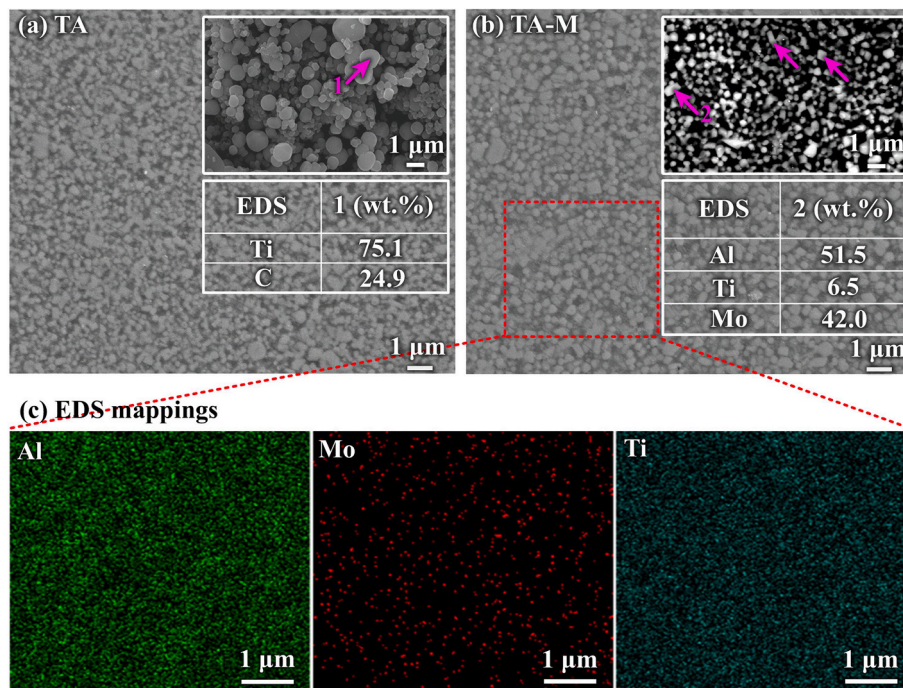


Fig. 2. SEM micrographs for the (a) TA and (b) TA-M. (c) EDS mappings of the selected area in TA-M. The inset in (a) is the SEM micrograph and EDS of particles in TA. The inset in (b) is the back-scattered SEM micrograph and EDS of particles in TA-M.

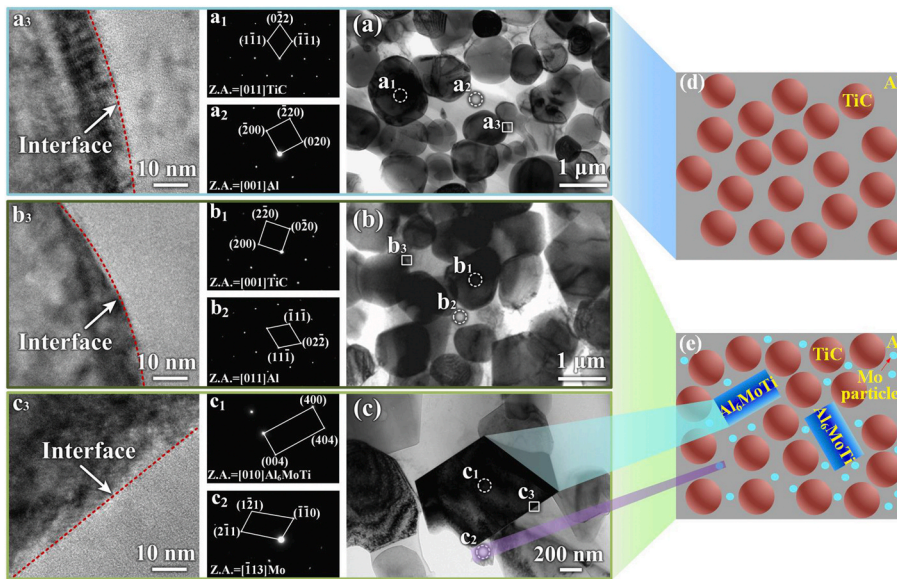


Fig. 4. (a) TEM micrographs of the TA, and the selected area electron diffraction (SAED) patterns at the region “a<sub>1</sub>” and “a<sub>2</sub>” and interface at the region “a<sub>3</sub>”; (b) TEM micrographs of the TA-M, and the SAED patterns at the region “b<sub>1</sub>” and “b<sub>2</sub>” and interface at the region “b<sub>3</sub>”; (c) TEM micrographs of the TA-M at high magnification, and the SAED at the region “c<sub>1</sub>” and “c<sub>2</sub>” and interface at the region “c<sub>3</sub>”; (d) and (e) the schematic diagram of microstructure configuration of the TA and TA-M, respectively.

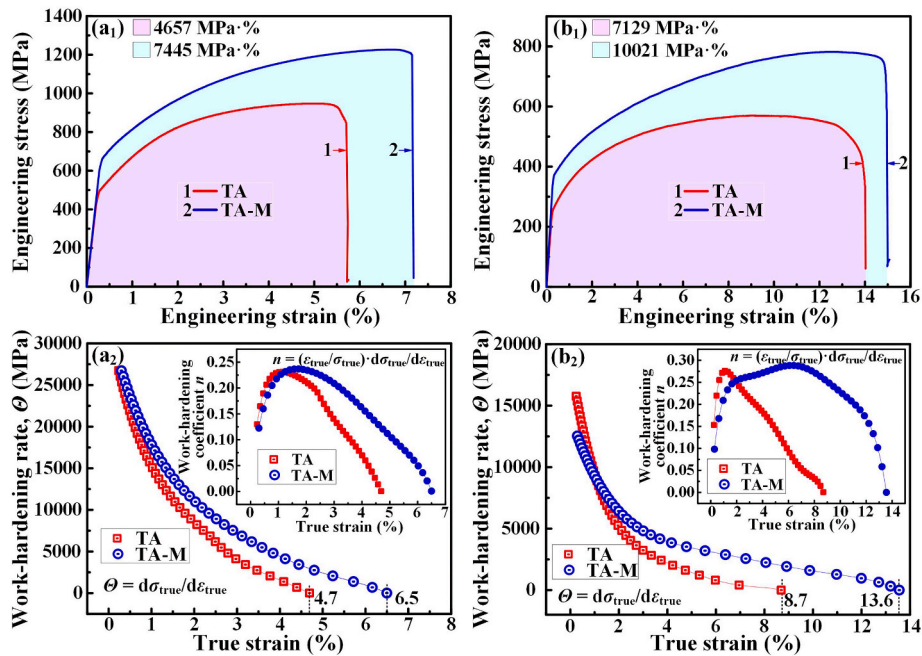


Fig. 5. Compressive engineering stress-strain curves, work-hardening rate  $\theta$  and work-hardening coefficient  $n$  of both cermet at (a<sub>1</sub>)-(a<sub>2</sub>) room temperature and (b<sub>1</sub>)-(b<sub>2</sub>) 573 K. The light pink area and light blue area in (a<sub>1</sub>) and (a<sub>2</sub>) represent the product of strength and plasticity of TA and TA-M. (For interpretation of the references to color in this figure legend, the reader is referred to the Web version of this article.)

Table 1

The mechanical properties of TA and TA-M.  $E$ : Young’s modulus;  $\sigma_{0.2}$ : yield strength;  $\sigma_{UCS}$ : ultimate compressive strength;  $\epsilon_f$ : fracture strain;  $\epsilon_p$ : plastic strain; UT: the product of strength and plasticity.

| Samples | $E$ (GPa) | Room temperature     |                      |                  |                  |            | 573 K                |                      |                  |                  |             |
|---------|-----------|----------------------|----------------------|------------------|------------------|------------|----------------------|----------------------|------------------|------------------|-------------|
|         |           | $\sigma_{0.2}$ (MPa) | $\sigma_{UCS}$ (MPa) | $\epsilon_f$ (%) | $\epsilon_p$ (%) | UT (MPa·%) | $\sigma_{0.2}$ (MPa) | $\sigma_{UCS}$ (MPa) | $\epsilon_f$ (%) | $\epsilon_p$ (%) | UT (MPa·%)  |
| TA      | 207 ± 7   | 545 ± 16             | 947 ± 23             | 5.8 ± 0.5        | 5.5 ± 0.6        | 4657 ± 361 | 283 ± 27             | 570 ± 31             | 14.0 ± 1.0       | 13.8 ± 0.8       | 7129 ± 411  |
| TA-M    | 218 ± 11  | 714 ± 21             | 1227 ± 19            | 7.2 ± 0.7        | 6.9 ± 0.9        | 7445 ± 339 | 392 ± 24             | 781 ± 29             | 15.3 ± 1.2       | 15.0 ± 1.1       | 10021 ± 389 |

from Table 1, the TA-M exhibits an ultimate compressive strength ( $\sigma_{UCS}$ ) and plastic strain ( $\epsilon_p$ ) at room temperature and 573 K respectively of 1227 MPa and 6.9%, 781 MPa and 15.0%, respectively, which are increased by ~30% and ~25%, ~37% and ~9%, respectively compared

with the corresponding ones (947 MPa and 5.5%, 570 MPa and 13.8%, respectively) for TA. Interestingly, the TA-M exhibits a superior product of strength and plasticity at room temperature (7445 MPa·%) and 573 K (10021 MPa·%), which are 60% and 41% respectively higher than those

of TA cermet (4657 MPa·%, 7129 MPa·%, respectively). To our knowledge, such an excellent combination of strength-plasticity in the Al-ceramic composites has not yet been achieved. Fig. 6 compares the  $\sigma_{UCS}$  and  $\epsilon_p$  for the Al-ceramic composites in this work and other reported [10,16,25,44–47]. One can note that the TA-M has higher  $\sigma_{UCS}$  and  $\epsilon_p$  compared with other Al-ceramic composites; particularly, TA-M demonstrates significantly higher strength-plasticity synergy than the nacre-inspired lamellar composites. Consequently, TA-M prepared in this work exhibits an outstanding balance of strength-plasticity.

The Young's moduli ( $E$ ) of the TA and TA-M are 207 and 218 GPa, which indicates that the  $Al_6MoTi$  and Mo particles have little effect on the stiffness of the cermets. Nevertheless, one can find that both cermets show apparently different work hardening. The work hardening rate ( $\theta$ ) of both cermets decreases rapidly with increasing the strain at room temperature and 573 K (Fig. 5a<sub>2</sub> and 5b<sub>2</sub>). However, the  $\theta$  of the TA-M shows slower decrease trend than that of the TA. Especially, the TA-M has a higher  $\theta$  of than TA at both 573 K when the true strain exceeds 2% and at room temperature. In addition, TA-M shows broader true strain ranges of work hardening (<6.5% at room temperature and <13.6% at 573 K) than TA (<4.7% at room temperature and <8.7% at 573 K). This indicates that TA-M has higher work hardening ability than TA. The work-hardening ability can be characterized by work-hardening coefficient ( $n$ ) (insets of Fig. 5a<sub>2</sub> and Fig. 5b<sub>2</sub>). The TA-M has apparently greater  $n$  than TA at both room temperature and 573 K. A high work hardening is usually caused by accumulation of dislocations, which promotes the strength-plasticity synergy of cermet [40,41,43,49]. Therefore, compatible deformation can be expected in the TA-M cermet.

### 3.3. Strengthening mechanism

Fig. 7a–d shows the SEM fracture surfaces of cermets. For TA, two main cracks and a lot of cracks with cataclastic characteristics are observed on the fracture surfaces of TA at room temperature and 573 K (Fig. 7a and b), respectively. Moreover, intact spherical particles and some holes on the magnified fracture surfaces of TA at room temperature and 573 K are observed (Fig. 7a<sub>1</sub> and Fig. 7b<sub>1</sub>), which indicates that the failure mode of TA is interfacial debonding. However, for TA-M, some fracture steps caused by crack deflection are found (Fig. 7c and d). In addition, the high-magnification images of the fracture surface display tear edges (Fig. 7c<sub>1</sub> and Fig. 7d<sub>1</sub>). Thus, the TA-M displays different failure mode compared to TA.

The schematic diagrams of strengthening and toughening mechanisms are given in Fig. 7e and f. As well known, dislocation gliding

produces good plasticity in pure Al. Because of almost no dislocation blocking accumulation, the work-hardening of Al is weak and hence deformation is unstable [43]. However, for the TA (Fig. 7e), a number of dislocations are presented near the interfaces due to crystallographic mismatch and difference in expansion coefficient between TiC ( $\sim 7.74 \times 10^{-6}/K$ ) and Al ( $\sim 23 \times 10^{-6}/K$ ) [26,48]. Under applied load, the dislocation gliding would encounter the ceramic particle barriers in a very short distance since Al layer is thinner, which results in a work hardening of TA. Unfortunately, the dislocation motion has difficulty to cut through and to bypass ceramic particles, while the stress concentration caused by dislocation accumulation would result in the formation of defects (which is the crack initiation i.e., the holes on fracture surfaces) at the interface (Fig. 7e<sub>1</sub> to Fig. 7e<sub>2</sub>). Afterward, cracks propagate along interface due to weak interface bonding and incompatibility between Al and TiC in plastic deformation, which leads to the failure of TA in the form of interfacial debonding. Meanwhile, the strain hardening terminates rapidly, which is the root of limited work hardening of the TA. In addition, the cracking and cataclastic characteristics on the fracture surface of TA indirectly indicate the load transfer effect is not smooth and the strain distribution is not uniform in the TA. Therefore, the TA presents highly localized deformation modes under applied stress and hence it possesses room for further enhancing its strength and plasticity.

In contrast, for the TA-M (Fig. 7f), first, the Mo has good wettability and strong interfacial bonding with TiC and  $Al_6MoTi$  [21], and the nanoscaled Mo particles distributed in Al can hinder dislocation glide. Second, compared to TA, the lattice distortion energy and dislocation density increase in TA-M, thereby rendering dislocations difficult to glide. Therefore, the work hardening is enhanced and the stress distribution becomes uniform in the cermet under applied load (Fig. 7f<sub>1</sub>). Third, the  $Al_6MoTi$  has good compatibility with TiC and Al because their property is compromised between brittle TiC and ductile Al and some loadings and deformation are transferred between TiC and Al. Under applied load, the stress concentration at the interfaces between  $Al_6MoTi$  and Al causes a small amount of deformation or even fracture of  $Al_6MoTi$ , since interface bonding between  $Al_6MoTi$  and Al is strong and  $Al_6MoTi$  has deformable nature. Therefore, the stress is released and deformation is transferred to a certain extent at the interface (Fig. 7f<sub>1</sub> and Fig. 7f<sub>2</sub>). As such, one can conclude that the  $Al_6MoTi$  and Mo particles successfully delocalize the stress concentration at heterogeneous phase interface. A uniform strain distribution and compatible deformation are formed in the cermet under loading. Hence, the TA-M possesses a significant enhancement in the strength-plasticity synergy.

### 4. Conclusions

This work successfully achieved unprecedented strength-plasticity synergy in a microstructure-designed 70 vol% (TiC +  $Al_6MoTi$  + Mo)/Al cermet with homogenous multiple length-scales microstructure. The cermet possesses including ultimate compressive strength of 1227 MPa and 781 MPa, plastic strain of 6.9% and 15.0%, the product of strength and plasticity of 7445 MPa·% and 10021 MPa·% at room temperature and 573 K respectively, which are enhanced by  $\sim 30\%$  and  $\sim 37\%$ ,  $\sim 25\%$  and  $\sim 9\%$ ,  $\sim 60\%$  and  $\sim 41\%$ , respectively, compared to traditional TiC/Al cermet. Such enhancement in strength-plasticity synergy is attributed to that the new microstructure configuration delocalizes the stress concentration at heterogeneous phase interface and to enhanced work hardening and compatible deformation in the cermet. Furthermore, the in-situ reaction hot-pressing method is a simple and cost-effective process to produce high volume reinforcement strengthened aluminium. The pioneering strategy proposed in this work shows the applicability to develop metal-ceramic composites with high strength and plasticity synergy, which opens new perspectives for the design and application of metal matrix composites.

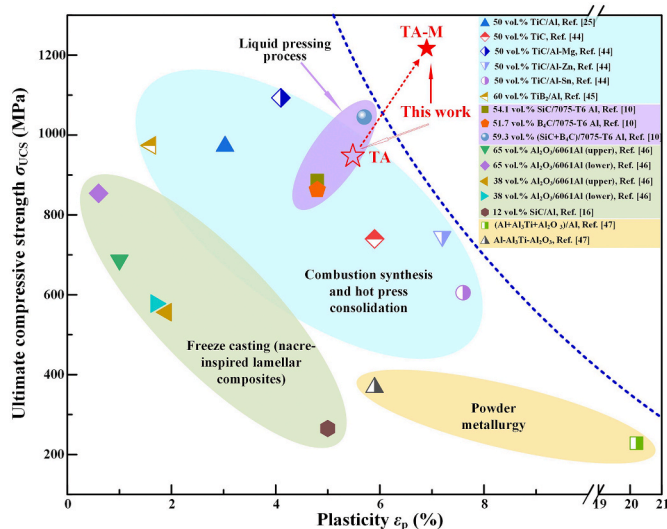


Fig. 6. Comparison of the strength-plasticity of Al-ceramic composites in this work and in literature.

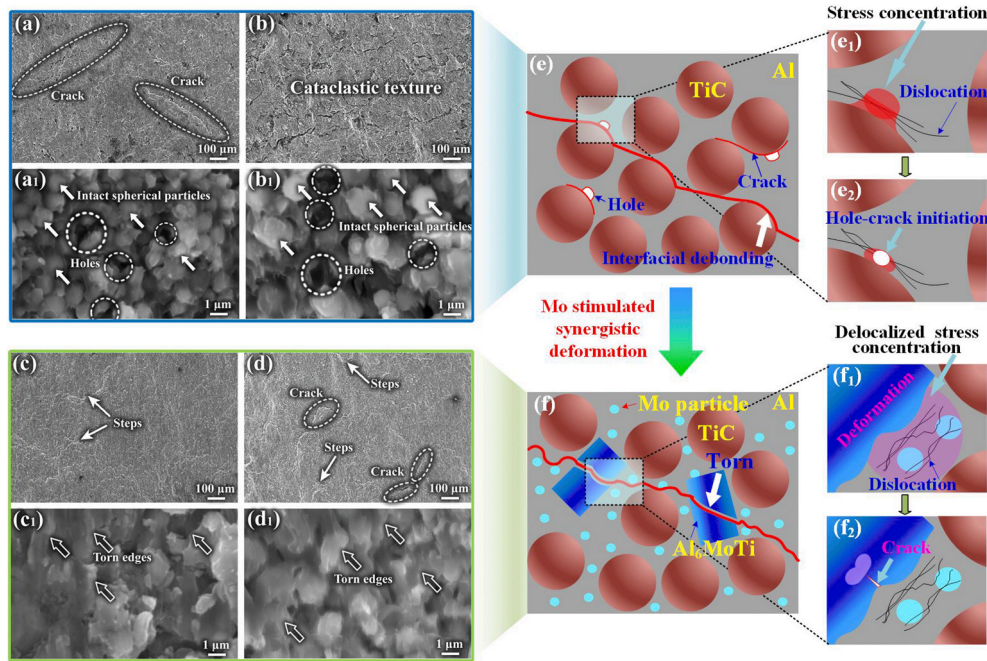


Fig. 7. SEM images of the overview and the magnified fracture surfaces of both cermets after compression testing: TA cermet (a) and (a<sub>1</sub>) at room temperature, (b) and (b<sub>1</sub>) at 573 K, TA-M cermet (c) and (c<sub>1</sub>) at room temperature, (d) and (d<sub>1</sub>) at 573 K. (e) and (f) schematic diagram of mechanisms of strengthening and toughening of the cermets.

#### Author statement

**Hong-Yu Yang:** Conceptualization, Project administration, Investigation, Visualization, Writing - original draft, Writing - review & editing. **Yi-Fan Yan:** Investigation, Visualization. **Tian-Shu Liu:** Investigation, Visualization. **Bai-Xin Dong:** Visualization. **Liang-Yu Chen:** Supervision, Writing - review & editing. **Shi-Li Shu:** Conceptualization, Data curation. **Feng Qiu:** Conceptualization, Project administration, Validation, Supervision, Resources. **Qi-Chuan Jiang:** Supervision. **Lai-Chang Zhang:** Conceptualization, Supervision, Writing - review & editing.

#### Declaration of competing interest

The authors declare that they have no known competing financial interests or personal relationships that could have appeared to influence the work reported in this paper.

#### Acknowledgements

This work was financially supported by the National Natural Science Foundation of China (No. 51971101, No. 51771081 and No. 51701086), the Postdoctoral Science Foundation of China (No. 2020M670849), and the 'thirteenth five-year plan' Science & Technology Research Foundation of Education Bureau of Jilin Province, China (No. JJKH20200971KJ).

#### References

- [1] Rong X, Zhang X, Zhao D, He C, Shi C, Liu E, et al. In-situ Al<sub>2</sub>O<sub>3</sub>-Al interface contribution towards the strength-ductility synergy of Al-CuO composite fabricated by solid-state reactive sintering. *Scripta Mater* 2021;198:113825.
- [2] Ren L, Xiao W, Kent D, Wan M, Ma C, Zhou L. Simultaneously enhanced strength and ductility in a metastable  $\beta$ -Ti alloy by stress-induced hierarchical twin structure. *Scripta Mater* 2020;184:6–11.
- [3] Xie X, Chen C, Chen Z, Wang W, Yin S, Ji G, et al. Achieving simultaneously improved tensile strength and ductility of a nano-TiB<sub>2</sub>/AlSi10Mg composite produced by cold spray additive manufacturing. *Compos B Eng* 2020;108404.
- [4] Zhai W, Zhu Z, Zhou W, Nai SML, Wei J. Selective laser melting of dispersed TiC particles strengthened 316L stainless steel. *Compos B Eng* 2020;199:108291.

- [5] Cao H, Su Y, Zhang D, Ouyang Q. Fabrication, mechanical and thermal behaviors of antiperovskite manganese nitride Mn<sub>3</sub>12N<sub>0.5</sub>Sn<sub>0.4</sub>N reinforced aluminum matrix composites. *Compos B Eng* 2021;223:109080.
- [6] Kai X, Wu L, Peng Y, Tan Z, Li G, Chen G, et al. Effects of Zr element on the microstructure and mechanical properties of B<sub>4</sub>C/Al composites fabricated by melt stirring method. *Compos B Eng* 2021;224:109156.
- [7] Wolf W, Bolfarini C, Kiminami CS, Botta WJ. Fabrication of Al-matrix composite reinforced with quasicrystals using conventional metallurgical fabrication methods. *Scripta Mater* 2019;173:21–5.
- [8] Wolf W, e Silva Lp M, Zepon G, Kiminami CS, Bolfarini C, Botta WJ. Single step fabrication by spray forming of large volume Al-based composites reinforced with quasicrystals. *Scripta Mater* 2020;181:86–91.
- [9] Nie J, Chen Y, Chen X, Liu X, Liu G, Zhao Y, et al. Stiff, strong and ductile heterostructured aluminum composites reinforced with oriented nanoplatelets. *Scripta Mater* 2020;189:140–4.
- [10] Jo MC, Choi JH, Yoo J, Lee D, Shin S, Jo I, et al. Novel dynamic compressive and ballistic properties in 7075-T6 Al-matrix hybrid composite reinforced with SiC and B<sub>4</sub>C particulates. *Compos B Eng* 2019;174:107041.
- [11] Park B, Lee D, Jo I, Lee SB, Lee SK, Cho S. Automated quantification of reinforcement dispersion in B<sub>4</sub>C/Al metal matrix composites. *Compos B Eng* 2020;181:107584.
- [12] Lei YB, Wang ZB, Zhang B, Luo ZP, Lu J, Lu K. Enhanced mechanical properties and corrosion resistance of 316L stainless steel by pre-forming a gradient nanostructured surface layer and annealing. *Acta Mater* 2021;208:116773.
- [13] Li Q, Yan FK, Tao NR, Ponge D, Raabe D, Lu K. Deformation compatibility between nanotwinned and recrystallized grains enhances resistance to interface cracking in cyclic loaded stainless steel. *Acta Mater* 2019;165:87–98.
- [14] Xiong L, You ZS, Qu SD, Lu L. Fracture behavior of heterogeneous nanostructured 316L austenitic stainless steel with nanotwin bundles. *Acta Mater* 2018;150:130–8.
- [15] Guo R-F, Wang Y, Shen P, Shaga A, Ma Y-H, Jiang Q-C. Influence of matrix property and interfacial reaction on the mechanical performance and fracture mechanism of TiC reinforced Al matrix lamellar composites. *Mater Sci Eng, A* 2020;775:138956.
- [16] Guo N, Shen P, Guo R-F, Jiang Q-C. Optimization of the properties in Al/SiC composites by tailoring microstructure through gelatin freeze casting. *Mater Sci Eng, A* 2019;748:286–93.
- [17] Avci U, Temiz Ş. A new approach to the production of partially graded and laminated composite material composed of SiC-reinforced 7039 Al alloy plates at different rates. *Compos B Eng* 2017;131:76–81.
- [18] Yang L-K, Shen P, Guo R-F, Li Y-L, Jiang Q-C. A novel strategy for fabricating biomimetic gradient metal-ceramic composites by dynamic freeze casting and pressure infiltration. *Scripta Mater* 2019;167:101–4.
- [19] Geng J, Li Y, Xiao H, Wang Z, Wang M, Chen D, et al. Deformation-induced ultrafine grains near fatigue crack tip and correlative fatigue damage in Al matrix composite. *Scripta Mater* 2021;193:49–54.
- [20] Amirian B, Li HY, Hogan JD. The mechanical response of a  $\alpha_2$ (Ti<sub>3</sub>Al) +  $\gamma$ (TiAl)-submicron grained Al<sub>2</sub>O<sub>3</sub> cermet under dynamic compression: modeling and experiment. *Acta Mater* 2019;181:291–308.

- [21] Wang H, Harrington T, Zhu C, Vecchio KS. Design, fabrication and characterization of FeAl-based metallic-intermetallic laminate (MIL) composites. *Acta Mater* 2019; 175:445–56.
- [22] Sun M-Q, Shen P, Jiang Q-C. Microstructures and mechanical characterizations of high-performance nacre-inspired Al/Al<sub>2</sub>O<sub>3</sub> composites. *Compos Part A-Appl S* 2019;121:465–73.
- [23] Hu Z-J, Guo R-F, Chen S-M, Jin Q, Shen P. Synthesis of damage-tolerant Cu-matrix composites with nacre-inspired laminate-reticular hierarchical architecture via tuning compositional wettability. *Scripta Mater* 2020;186:312–6.
- [24] Radi K, Jauffres D, Deville S, Martin CL. Strength and toughness trade-off optimization of nacre-like ceramic composites. *Compos B Eng* 2020;183:107699.
- [25] Yang H-Y, Wang Z, Chen L-Y, Shu S-L, Qiu F, Zhang L-C. Interface formation and bonding control in high-volume-fraction (TiC+TiB<sub>2</sub>)/Al composites and their roles in enhancing properties. *Compos B Eng* 2021;209:108605.
- [26] Dong B-X, Li Q, Wang Z-F, Liu T-S, Yang H-Y, Shu S-L, et al. Enhancing strength-ductility synergy and mechanisms of Al-based composites by size-tunable in-situ TiB<sub>2</sub> particles with specific spatial distribution. *Compos B Eng* 2021;217:108912.
- [27] Radi K, Saad H, Jauffres D, Meille S, Douillard T, Deville S, et al. Effect of microstructure heterogeneity on the damage resistance of nacre-like alumina: insights from image-based discrete simulations. *Scripta Mater* 2021;191:210–4.
- [28] Alghamdi S, Du F, Yang J, Pinder G, Tan T. Tensile and shear behavior of microscale growth layers between nacre in red abalone. *J Mech Phys Solid* 2020; 138:103928.
- [29] Yang HY, Wang Z, Yue X, Ji PJ, Shu SL. Simultaneously improved strength and toughness of in situ bi-phased TiB<sub>2</sub>-Ti(C,N)-Ni cermets by Mo addition. *J Alloys Compd* 2020;820:153068.
- [30] Kriegel MJ, Walnsch A, Distl B, Fabrichnaya O, Freudenberger J, Leineweber A. The ternary Al–Mo–Ti system revisited: phase equilibria of Al63(Mo,Ti)37. *J Alloys Compd* 2019;811:152055.
- [31] Rong X, Zhao D, He C, Shi C, Liu E, Zhao N. Revealing the strengthening and toughening mechanisms of Al-CuO composite fabricated via in-situ solid-state reaction. *Acta Mater* 2021;204:116524.
- [32] Rabadia CD, Liu YJ, Zhao CH, Wang JC, Jawed SF, Wang LQ, et al. Improved trade-off between strength and plasticity in titanium based metastable beta type Ti-Zr-Fe-Sn alloys. *Mater Sci Eng, A* 2019;766:138340.
- [33] Jawed SF, Rabadia CD, Liu YJ, Wang LQ, Qin P, Li YH, et al. Strengthening mechanism and corrosion resistance of beta-type Ti-Nb-Zr-Mn alloys. *Mater Sci Eng C* 2020;110:110728.
- [34] Liu T-S, Qiu F, Dong B-X, Geng R, Zha M, Yang H-Y, et al. Role of trace nanoparticles in establishing fully optimized microstructure configuration of cold-rolled Al alloy. *Mater Des* 2021;206:109743.
- [35] Qiu F, Zhang H, Li C-L, Wang Z-F, Chang F, Yang H-Y, et al. Simultaneously enhanced strength and toughness of cast medium carbon steels matrix composites by trace nano-sized TiC particles. *Mater Sci Eng, A* 2021;819:141485.
- [36] Zhang MX, Kelly PM. Edge-to-edge matching and its applications: Part I. Application to the simple HCP/BCC system. *Acta Mater* 2005;53(4):1073–84.
- [37] Zhang MX, Kelly PM. Edge-to-edge matching and its applications: Part II. Application to Mg–Al, Mg–Y and Mg–Mn alloys. *Acta Mater* 2005;53(4):1085–96.
- [38] Zhang M, Kelly P, Easton M, Taylor J. Crystallographic study of grain refinement in aluminum alloys using the edge-to-edge matching model. *Acta Mater* 2005;53(5): 1427–38.
- [39] Zhang MX, Kelly PM, Qian M, Taylor JA. Crystallography of grain refinement in Mg–Al based alloys. *Acta Mater* 2005;53:3261–70.
- [40] Lu K, Lu L, Suresh S. Strengthening materials by engineering coherent internal boundaries at the nanoscale. *Science* 2009;324:349–52.
- [41] Zhao YH, Liao XZ, Cheng S, Ma E, Zhu YT. Simultaneously increasing the ductility and strength of nanostructured alloys. *Adv Mater* 2006;18(17):2280–3.
- [42] Zhao YH, Zhu YT, Lavernia EJ. Strategies for improving tensile ductility of bulk nanostructured materials. *Adv Eng Mater* 2010;12:769–78.
- [43] Zhu YT, Wu XL. Ductility and plasticity of nanostructured metals: differences and issues. *Mater Today Nano* 2018;2:15–20.
- [44] Shu S, Lu J, Qiu F, Xuan Q, Jiang Q. Effects of alloy elements (Mg, Zn, Sn) on the microstructures and compression properties of high-volume-fraction TiC<sub>x</sub>/Al composites. *Scripta Mater* 2010;63(12):1209–11.
- [45] Zhang L, Xuan Q, Wang J, Qiu F, Jiang Q. Effects of TiB<sub>2</sub> content and alloy elements (Mg, Mo, V) on the compression properties of high-volume-fraction TiB<sub>2</sub>/Al composites. *Mater Sci Eng, A* 2014;607:28–32.
- [46] Li Y-L, Shen P, Yang L-K, Sun X, Jiang Q-C. A novel approach to the fabrication of lamellar Al<sub>2</sub>O<sub>3</sub>/6061Al composites with high-volume fractions of hard phases. *Mater Sci Eng, A* 2019;754:75–84.
- [47] Lakra S, Bandyopadhyay TK, Das S, Das K. Synthesis and characterization of in-situ (Al–Al<sub>3</sub>Ti–Al<sub>2</sub>O<sub>3</sub>)/Al dual matrix composite. *J Alloys Compd* 2020;842:155745.
- [48] Gao Y-Y, Dong B-X, Qiu F, Geng R, Wang L, Zhao Q-L, et al. The superior elevated-temperature mechanical properties of Al-Cu-Mg-Si composites reinforced with in situ hybrid-sized TiC<sub>x</sub>-TiB<sub>2</sub> particles. *Mater Sci Eng, A* 2018;728:157–64.
- [49] Chen L-Y, Cui Y-W, Zhang L-C. Recent development in beta titanium alloys for biomedical applications. *Metals* 2020;10(9):1139.